Processing and Application of Ceramics 16 [4] (2022) 391–401
https://doi.org/10.2298/PAC2204391S

Development of a new system of solid ionic conductors based on multi-doped ceria for application in IT-SOFCs

Marija Stojmenović[1,*], Neda Nišić[1], Milan Žunić[2], Francesco Basoli[3], Jelena Gulicovki[1], Ivica Ristović[4], Milan Kragović[1]

[1] *"Vinča" Institute of Nuclear Sciences, National Institute of the Republic of Serbia, University of Belgrade, 11351 Belgrade, Serbia*
[2] *Institute for Multidisciplinary Research, University of Belgrade, Kneza Viseslava 1, 11000 Belgrade, Serbia*
[3] *Department of Engineering, Università Campus Bio-Medico di Roma, Via Álvaro del Portillo 21, 00128 Rome, Italy*
[4] *Faculty of Mining and Geology, Đušina 7, 11000 Belgrade, University of Belgrade, Serbia*

Received 13 June 2022; Received in revised form 21 October 2022; Accepted 4 November 2022

Abstract

Nanosized multi-doped ceria with composition $Ce_{0.8}Nd_{0.0025}Sm_{0.0025}Gd_{0.005}Dy_{0.095}Y_{0.095}O_{2-\delta}$ (CNSGDY) as perspective solid ionic conductor was obtained by modified glycine-nitrate procedure (MGNP) and room temperature self-propagating reaction (SPRT). The pressed pellets of both powders were sintered at 1550 °C for 2 h in an air atmosphere. The obtained sintered samples were characterized by XRPD, Raman spectroscopy, FESEM, EDS and EIS methods. Despite a high temperature of sintering, XRPD and FESEM analyses of the samples confirmed appropriate dimensions of grains with fluorite structure. Overall concentration of introduced dopants (x = 0.2) in the structure of CeO_2 after the sintering process was confirmed by EDS analysis. After sintering, Raman spectroscopy confirmed retention of the oxygen vacancies in the ceria lattice, which is in accordance with the improvement of ionic conductivity of solid ionic conductors. The highest value of total conductivity was obtained for the sintered MGNP sample at 700 °C (4.22×10^{-2} S cm^{-1}), with the corresponding activation energy of 0.26 eV.

Keywords: *CeO_2, sintering, electrical conductivity, impedance spectroscopy, fuel cells*

I. Introduction

Cerium(IV) oxide (CeO_2) based materials have found multiple applications in different industry fields, such as electronics [1,2], environmental protection [3,4], optics [4,5], catalysis [6–10] and clean energy [11,12], which is the reason why CeO_2 is receiving considerable interest of the scientific community, constantly increasing over the last decade. Particular attention has recently been devoted to the development of next-generation power production system - solid oxide fuel cells (SOFC), which present devices operating with a supply of fuel that can provide sustainable, environmentally-friendly and efficient energy conversion and electricity generation with superior lifetime for widespread necessities [11–16]. The yttrium stabilized zirconia presents so far the most common reliable electrolyte material, considering its superior oxygen ion conductivity at high temperatures characteristic for conventional SOFC operation (800–1000 °C) [17,18]. However, such high working temperatures lead to several disadvantages referring to technical complications in the first place. Thermal breakdown and mismatch of cell components, reduction of reliability over time, thermal stresses affecting cell structure and integrity and limited choice of fabrication materials are some of them [15–17,20]. In addition, there are substantial financial issues concerning manufacturing and operation costs. Therefore, in order to facilitate materials selection, prevent the cell component degradation and increase overall cost reduction there is a tendency among SOFC community toward lowering of operation temperatures into an intermediate range (600–800 °C), without negative impact

* Corresponding author: tel: +381 11 3408860
e-mail: *mpusevac@vin.bg.ac.rs*

on high oxygen reduction reaction kinetics while maintaining high ionic conductivity [15].

In order to meet the mentioned criteria, an appropriate choice of electrolyte constituents is found to be of utmost importance. Consequently, a great deal of research has put ceria based materials in the spotlight, considering their favourable properties such as relatively high ionic conductivity with low activation energies at reduced temperatures of IT-SOFC (600–800 °C), much higher in comparison to conventionally used YSZ [17,19,20]. As a result, enormous effort has been made on progress in the development of a newly improved type of electrolyte materials containing pure, co- or multi-doped ceria since it may be the vital global challenge when it comes to commercialization of these newly generated IT-SOFCs (intermediate temperature solid oxide fuel cells) operating with high efficiency at temperatures below 800 °C. Additionally, in plenty of research work, the focus has been placed on future production of ceria based ceramic powders as solid conductors with the implementation of less expensive technologies including less complex methodology frames [21–23].

In order to develop optimal compositions that will fulfil the mandatory criteria for applications in IT-SOFC technology, many issues need to be tackled, mainly relating to the optimal selection of: i) electrolyte and dopants, ii) methods for synthesis of starting powders and iii) the densification process.

As convenient starting ultrafine nanopowder intended for the production of ceramic electrolytes in IT-SOFCs, CeO_2 doped with different trivalent rare earth such as Nd, Sm, Gd, Dy and Y provides increased ionic conductivity [14,17,21,24]. Namely, the formation of oxygen vacancies ($V^{\cdot\cdot}$) in the cerium lattice allows to achieve the high ionic conductivity at lower temperatures, due to the replacement of Ce^{4+} ions with rare earth (III)-valent ions as dopants for the purpose of the compensation of the charge balance in the lattice [25,26].

Furthermore, the method that provides the necessary properties of the starting powders and has a lot of advantages in comparison to conventional methods [27–29] is obtained by a combination of modified glycine-nitrate procedure (MGNP method) [21–24] and room temperature self-propagating reaction (SPRT method) [21–23]. These methods are simultaneously very fast and reliable, and contrary to other methods [27–29], require extremely simple and inexpensive equipment which contributes to the cost effectiveness of the process. Partial replacement of nitrate with acetate ions in the MGNP procedure allows better control of the chemical reaction while the SPRT procedure allows the occurrence of the spontaneous self-propagating reaction between metal nitrates and sodium hydroxide at room temperature, with extremely fast termination. These methods provide very precise stoichiometry of the final products compared with a tailored composition and achieve very high yields (96–99%) [18–20].

In addition, for oxygen ion conducting solid oxides it is very important for the electrolyte layer to be fully dense. Therefore, a densification process is required to provide sintered samples obtained from powders synthesized by MGNP and SPRT methods that possess desirable microstructure with smaller grains and more uniform size distribution. This is needed in order to mitigate the cross-over of unreacted fuel or oxidant through the electrolyte and to allow a sufficient connection for oxygen ion diffusion [20]. Densification requires a high temperature of sintering, however, the right selection of this process may present a significant precondition for a considerable decrease in this temperature and for reducing energy losses in the process of fuel cells production.

Synthesis and complete characterization of nanopowder complex composition $Ce_{0.8}Nd_{0.0025}Sm_{0.0025}Gd_{0.005}Dy_{0.095}Y_{0.095}O_{2-\delta}$ (CNSGDY), obtained by MGNP and SPRT method, has already been performed with results presented in our previous article [26]. In the present study, properties of multi-doped ceramic electrolytes of the identical composition obtained from nanopowders synthesized by the same procedures (MGNP and SPRT) were investigated after densification under sintering at 1550 °C for 2 h in air atmosphere. The sintered samples of MGNP and SPRT produced powders were analysed in a comparative manner with an emphasis on their potential application in IT-SOFCs as perspective solid ionic conductors. Despite sintering temperature as high as 1550 °C, the overall mole fraction of dopants was kept constant ($x = 0.2$). The dopant concentration was determined based on the previous literature reports, which found that the optimum lies within the range of 10–20 mol% for many cations in fluorite ceria lattice enabling the achievement of the highest possible ionic conductivity [22–24,30–34].

The aim of the present study was the estimation of usability of nanosized solid electrolyte doped ceria with composition CNSGDY ($x = 0.2$) obtained with either SPRT or MGNP methods as a perspective electrolytes for IT-SOFC with potentially high oxygen ion conductivity, low polarization resistance and good compatibility with adjoining components, i.e. electrodes. All things considered, the present research efforts are aimed toward the optimization of IT-SOFCs overall performance and improvement of vital features referring to high efficiency at low operating temperatures, reasonably low fabrication and maintenance expenses and eco-friendliness in terms of the absence of pollutants and utilization of renewable energy resources as fuel. In that manner, the results of this study may greatly contribute to the global expansion and commercialization of IT-SOFCs.

II. Experimental

The initial compositions of solid solutions were calculated based on the ion-packing model [35]. This

model was applied for the calculation of the fraction of constituting ion dopants providing the lattice parameter close to that of pure ceria, in order to maintain the stability of the crystal lattice. The following equation was used for the determination of lattice parameters of solid electrolytes with fluorite structure, based on the ion-packing model:

$$a_{jpm} = \frac{4}{\sqrt{3}}\left[xr_M + (1-x)r_{\mathrm{Ce}} + (1-0.25x)r_{\mathrm{O}} + 0.25xr_{V_{\ddot{\mathrm{O}}}}\right]0.9971 \quad (1)$$

where a_{jpm} is the lattice parameter, r_M, r_{Ce}, r_{O} and $r_{V_{\ddot{\mathrm{O}}}}$ are the radii of the dopant cations (Nd^{3+}, Sm^{3+}, Gd^{3+}, Dy^{3+} and Y^{3+}), cerium ion Ce^{4+} (0.97 Å), oxygen ion O^{2-} (1.38 Å) and oxygen vacancy radius $V_{\mathrm{O}}^{\ddot{}}$ (1.164 Å), respectively; x is the dopant molar fraction [35]. The correction factor, 0.9971, accounts for the observed difference in the experimental value and the value calculated from the ionic radii for the lattice parameter of pure ceria [35]. Lattice parameter (a_{jpm}) of pure ceria obtained by SPRT method is 5.4114 Å [21].

2.1. Synthesis by MGNP method

Synthesis of the nanosized powder with the CNSGDY composition by MGNP method was performed with the following initial components: an aqueous solution of δ-amino acetic acid-glycine (NH_2CH_2COOH) (Fluka), a solution of $Ce(NO_3)_4$ and $Ce(CH_3COO)_4$, mixed in a mole ratio 1:1, and a solution of nitrates formulated as $[Me(NO_3)_3 \cdot 6\,H_2O]$, with Nd, Sm, Gd, Dy and Y (Aldrich, USA) standing for Me. All dissolved compounds were added in the exact amounts, which were needed for obtaining a total dopant concentration of 20 mol% of the final product ($x = 0.2$) [26]. For initiation of the reaction, a thoroughly cleaned steel reactor was used. Primarily, all reactants were completely dissolved in distilled water and after that simultaneously poured into the reactor [26]. In order to adjust the required metal nitrate concentration and obtain the targeted final doped powder [26], the calculation was made with the equation presented below:

$$4\,NH_2CH_2COOH + 2\left[(1-x)Ce(NO_3)_3 \cdot 6\,H_2O + xMe(NO_3)_3 \cdot 6\,H_2O\right] + 2\,O_2 \longrightarrow 2\,Ce_{1-x}Me_xO_{2-\delta} + 22\,H_2O\uparrow + 5\,N_2\uparrow + 8\,CO_2\uparrow \quad (2)$$

Firstly, heating was performed at 90 °C for the purpose of removal of excess water from the prepared solution and then further at 540 °C in order to cause glycine ignition followed by decomposition of nitrates and acetate. Afterwards, the calcination process was carried out at 600 °C over a period of 2 h to eliminate any remaining organic components [26]. In MGNP process, cerium nitrate was partially replaced with acetate salt which significantly slowed down the reaction and prevented losses of the reactants by sprinkling. The quantity of such experimentally obtained powder was very close to theoretically calculated values (96–99%) and noticeably higher compared to quantities that could be provided with the application of other relevant methodologies [22–24,26].

2.2. Synthesis by SPRT method

Nanopowder of the above mentioned composition was also synthetized using SPRT method [13]. Starting reactants involved in this process were NaOH (Vetprom chemicals) and nitrate salts of Ce, Nd, Sm, Gd, Dy and Y (Aldrich, USA). The quantity of reactants in this reaction was determined using the following equation [26]:

$$2[(1-x)\,Ce(NO_3)_3 \cdot 6\,H_2O + xMe(NO_3)_3 \cdot 6\,H_2O] + 6\,NaOH + (1/2-\delta)\,O_2 \longrightarrow 2\,Ce_{1-x}Me_xO_{2-\delta} + 6\,NaNO_3 + 15\,H_2O \quad (3)$$

Initially, reactants were carefully blended in an alumina mortar for 15 min, which enabled the acceleration of the reaction at room temperature in the air [26]. Additional air-drying of the mixture for about 3 h provided the end of the reaction in accordance with Eq. 3. Later, the obtained suspension was transferred to the test tube filled with a certain amount of distilled water and centrifuged (Centurion 1020D centrifuge) at 3000 rpm, for 10 min. The samples were rinsed four times in water as well as twice in ethanol. Finally, the synthesized nanopowder was dried at 100 °C. These procedure steps resulted in reaching the expected stoichiometry of the powder. The essence and the major advantage of this method is yielding the ceramic powders at almost room temperature by an exothermic solid-state reaction which explains why this method is much more cost-effective in comparison to the others [26–29].

2.3. Characterization of samples after sintering

Characterization of the nanopowders with the composition CNSGDY obtained by MGNP and SPRT methods was presented in our previous study [26]. For the purpose of the present research, a part of the obtained powdery samples was isostatically pressed into discs of 8 mm in diameter and of approximately 0.5 mm in thickness under a pressure of 225 MPa and subjected to densification under a sintering process at 1550 °C in air atmosphere for 2 h in a high temperature furnace. Afterwards, the sintered samples were characterized using X-ray powder diffraction (XRPD), Raman spectroscopy, field emission-scanning electron microscopy (FESEM) and energy dispersive X-ray spectroscopy (EDS) as characterization tools. Potential application of the obtained sintered samples after the densification process as electrolyte materials in SOFCs was examined by the complex electrochemical impedance method (EIS).

For X-ray powder diffraction (XRPD) with $CuK\alpha_{1,2}$ radiation, the device Ultima IV Rigaku diffractometer equipped with a voltage generator (40.0 kV) and a current generator (40.0 mA) was used [26]. The 2θ range

of 20–80° was applied for all synthesized powders in a continuous scan mode with a scanning step size of 0.02° and at a scan rate of 2 °/min [26]. Prior to the measurements, high quality Si standard was used in terms of the angular correction. The least square procedure was performed to refine lattice parameters from the available data. The standard deviation was about 1%. Estimation of the internal microstrain in the samples was carried out based on the Williamson-Hall plots which were formed applying the formula [14,19–21]:

$$\beta_{total} \cdot \cos\theta = \frac{0.9\lambda}{D} + \frac{4\Delta d}{d}\sin\theta \qquad (4)$$

where β_{total} is the full width at half maximum of the XRPD peak, λ is the incident X-ray wavelength, θ is the diffraction angle, D is the crystallite size and Δd is the difference of the d spacing corresponding to a typical peak.

XDR Raman microscope (Thermo Scientific, USA), equipped with an Olympus optical microscope and a CCD detector was used for collecting Raman spectra excited with a diode pumped solid state high-brightness laser (532 nm) [26]. The measurements were conducted in the spectral range of 200–800 cm^{-1} at ambient temperature [26]. The powder was placed on X-Y motorized sample stage. The laser beam of an objective magnification ×10k was focused on the sample. The spectrograph with a grating of 900 lines/mm was used for analysis of the scattered light while laser power was kept at 1 mW.

For the purpose of scanning electron microscopy (SEM) analysis, the electron microscope model FE-SEM JEOL JSM 6330F (Japan) was used [26]. Prior to observation, the samples were pre-coated with a layer of gold of only several nanometres thickness. The coating procedure was carried out using Fine Coat JFC-1100 ION SPUTTER (Company JEOL) device. Images were recorded in SEI mode at a magnification of ×10k with the accelerating voltage of 10 kV [26]. EDS analysis was performed at the invasive electron energy of 30 keV by means of QX 2000S device, a product of the company Oxford Microanalysis Group with a maximum resolution of 0.4 nm [26].

The electrical properties of the sintered CNSGDY samples were measured by the complex impedance method, in a frequency range of 10 μHz–1 MHz, using Interface 1000 Potentiostat/Galvanostat/ZRA and EIS300 electrochemical impedance spectroscopy Software (EIS). The measurements were conducted in air, in the temperature range of 500–700 °C, with 50 °C increment. The amplitude of the applied sinusoidal voltage signal was 20 mV [23,24]. A thin layer of high conductivity silver paste was applied onto both sides of the sample pellets, in order to provide good electrical contact between electrolyte and electrodes. The samples were placed between silver plates in a ceramic holder, which was heated by the vertical oven. A Pt-Rh thermocouple located just below the bottom silver plate was used for temperature monitoring [23,24]. Experimentally obtained impedance plots were fitted by using software ZView for Windows (Version 3.2b). The resistance values were determined from the impedance diagrams recorded at various temperatures. The specific conductance was calculated from the resistance data based on the dimensions of the sample pellets [23,26].

III. Results and discussion

3.1. Structure details of nanopowders

X-ray diffraction patterns of the multi-doped sintered samples obtained from the nanopowders synthesized by MGNP and SPRT methods are presented in Fig. 1a. From XRPD results, it may be observed that for the investigated samples the single phase of ceria with a cubic fluorite structure and the space group *Fm3m* (No: 01-081-0792, PDF2 release database, 2012) was formed [26], similar to pure CeO_2 [21], without any other traces or secondary phases. This means that the CeO_2 was fully stabilized by Nd_2O_3, Sm_2O_3, Gd_2O_3, Dy_2O_3 and Y_2O_3, despite the high temperature of the sintering process (1550 °C) [26]. Thus, sintered samples as final products, i.e. solid ionic conductors, retained

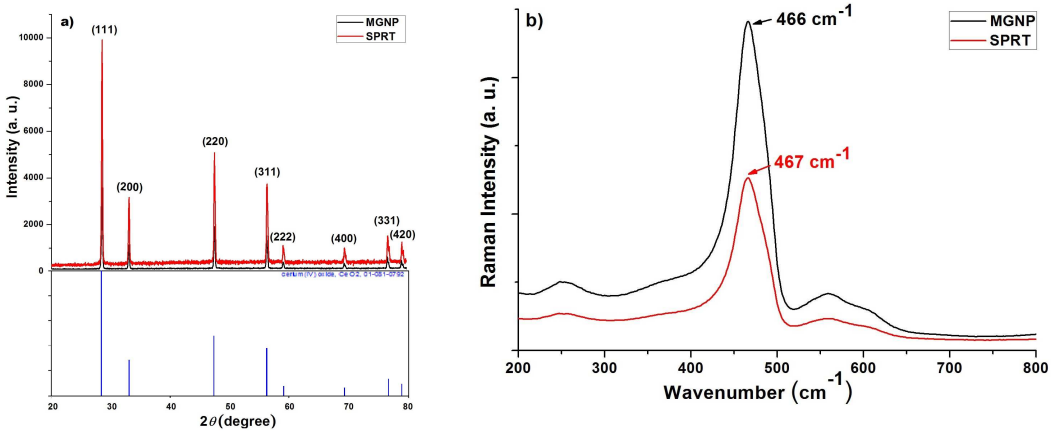

Figure 1. X-ray diffraction patterns (a) and Raman spectra (b) of sintered CNSGDY samples obtained by MGNP and SPRT methods

Table 1. Lattice parameter obtained by ion-packing model (a_{jpm}) and lattice parameter (a_{XRPD}), crystallite size (D_{XRPD}) and microstrain (e_{XRPD}) obtained by XRPD analysis for sintered samples CNSGDY obtained by MGNP and SPRT methods

Composition	a_{jpm} [Å]	a_{XRPD} [Å]	D_{XRPD} [nm]	e_{XRPD} [%]
CNSGDY (MGNP method)	5.4012	5.4004	41.31	1.72
CNSGDY (SPRT method)	5.4015	5.4009	33.52	2.26

the same structural features as the starting powder [26], which confirmed that dopant ions with oxidation number 3+ successfully replaced the Ce^{4+} ions in the crystal lattice of the CeO_2.

Since it is considered a useful tool for indication of electrical conductivity behaviour, lattice parameter was experimentally measured for the multi-doped ceria nanopowders obtained by both MGNP and SPRT methods after the synthesis process [26], as well as after the sintering process (Table 1), by means of XRPD analysis. After sintering, a decrease in lattice parameters of the multi-doped CNSGDY sintered samples was recorded (5.4004 Å for MGNM and 5.4009 Å for SPRT; Table 1), which indicated a good atomic arrangement in the crystal lattice [26]. Specifically, applying the equation used for the determination of lattice parameters (a_{jpm}) of solid solution with fluorite structure, based on the ion-packing model [23,24], confirmed the agreement with values of a_{XRPD}. It was obvious that experimentally determined lattice parameter values for the doped sintered CeO_2 and pure sintered CeO_2 obtained by MGNP and SPRT methods agreed quite well (Table 1), which was the objective in this study [26]. Namely, the primary purpose of doping ceria with cations of lower valence was the introduction of oxygen vacancies into the crystal lattice of CeO_2, by replacing Ce^{4+} with trivalent dopants in order to achieve enhancement of ionic conductivity, while retaining the values of lattice parameter similar to pure CeO_2 [21].

The identification using the Raman spectrum, especially the Raman signature for O^{2-} vacancies is found to be essential for CeO_2-based solid electrolytes characterization. It is well established that pure and stoichiometric CeO_2 with fluorite structure has a single allowed Raman mode of the first order (with F_{2g} symmetry) with a position at 465 cm^{-1} [21,26], which is explained by the symmetric breathing mode of the oxygen around each cation (CeO_8, the lattice vibration). However, two additional Raman modes of the second order appeared, being positioned around 550 and 600 cm^{-1} [21–23,26]. Namely, the increase of the overall free sample surface as the consequence of particle size decrease enabled oxygen to release easier from the lattice, leaving the vacancy and two electrons localized on cerium atoms. This process led to the formation of Ce^{3+} ions, i.e. lowering of Ce^{4+} valence due to electroneutrality demand and the occurrence of the Raman mode at around 600 cm^{-1} [21–24,26]. On the other hand, for the doped samples, Raman mode at around 550 cm^{-1} originated from oxygen vacancies formed due to the replacement of Ce^{4+} ions with cations having a lower oxidation state (3+) [21–24,26]. As the literature suggests [23,24], the number of vacancies determined the intensity of these additional peaks and potential higher ionic conductivity may be assigned to their appearance (Fig. 1b). In this case, by using Raman spectroscopy, it was confirmed that sintered samples as final products, i.e. solid ionic conductors, retained the same structural features as the starting powder [26], which confirmed that dopant ions with oxidation number 3+ successfully replaced the Ce^{4+} ions in the crystal lattice of the CeO_2.

3.2. Densification and morphology

A higher densification level was obtained for the MGNP sintered samples, gaining 96 %TD while for the SPRT sintered samples only 89 %TD was reached. The theoretical density values were determined based on calculations found in the literature [21–24]. Such differences may be explained by different pore size distribution and particle size, which both play a significant role in achieving high density. Well-ordered structure, including only mesopores, more uniform particle size distribution caused by calcination for 4 h at 600 °C [21–24] and consequently better packing and lower inner activity, explained why for the MGNP sintered samples higher density was achieved, very close to theoretical one (Table 2). On the other hand, the samples obtained by the SPRT method were not subjected to calcination (according to the method) [21–24], which was the reason for the presence of mesopores and micropores in the structure. It was found that wide pore distribution in the samples may retard or inhibit the densification [23,24] since large pores tend to expand while small pores are likely to shrink and disappear during the sintering. Considering non-uniformity of particles, less compact particle packing, higher inner activity and a lot of vacancies present in the SPRT samples, a lower sintering density value was justified (Table 2) [23,24].

Table 2. Theoretical densities (ρ_{th}), Archimedes' densities (ρ_A) and relative densities (ρ_r) of sintered ceramic samples CNSGDY obtained by MGNP and SPRT methods

		MGNP		SPRT	
Composition	ρ_{th} [g/cm^3]	ρ_A [g/cm^3]	ρ_r [%TD]	ρ_A [g/cm^3]	ρ_r [%TD]
CNSGDY	7.22	6.72	96	6.22	89

It is worth noting that the above presented discussion of density results is in a good agreement with microstructural observations [23,24]. Scanning electron micrographs of the sintered CNSGDY samples prepared by MGNP and SPRT method are shown in Figs. 2a and 2b, respectively. Although the microstructures of both ceramic samples obtained from powders contain compact polygonal crystals, there is a noticeable difference depending on the applied synthesis method [21–

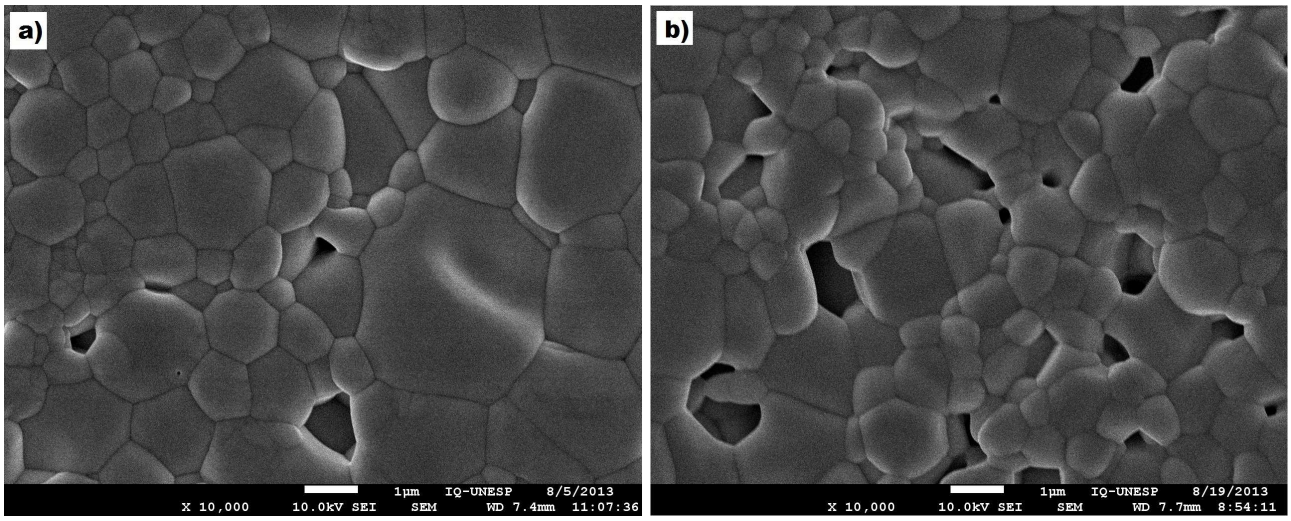

Figure 2. SEM micrographs of MGNP (a) and SPRT (b) sintered CNSGDY samples at 1550 °C for 2 h in an air atmosphere

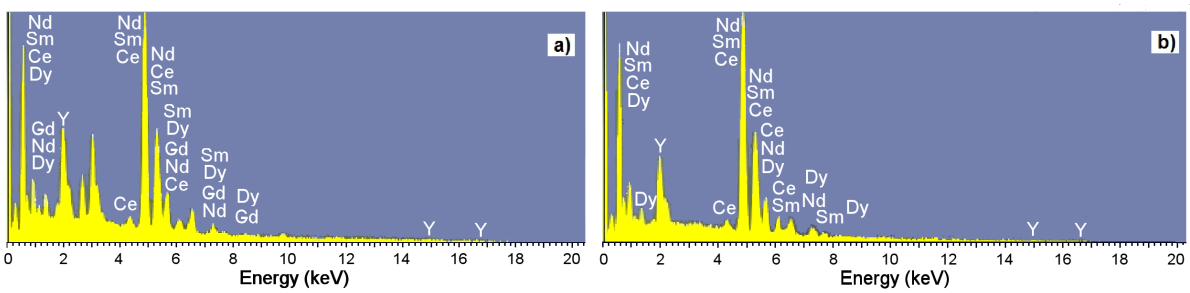

Figure 3. EDS spectra of MGNP (a) and SPRT (b) sintered CNSGDY samples at 1550 °C for 2 h in an air atmosphere

24]. Narrow grain size distribution and negligible porosity are characteristic of the sintered materials obtained from the MGNP powders (Fig. 2a) [21–24]. However, despite the good sintering of the MGNP samples, the fraction of small grains around larger grains indicates that the mechanism of Ostwald ripening has been responsible for most of the grain growth [22,24]. On the contrary, the ceramics obtained from the SPRT powders show a bimodal distribution with a significant amount of porosity (Fig. 2b). Besides, having noticed a certain number of curved grain boundaries it may be assumed that the sintering process of the samples in some points was not completely finished (Fig. 2b) [23,24]. The grain size was observed to be in the range of 1–4 µm. As it has already been stated, analysis of sample microstructure agrees with the fact that the different particle morphologies may affect density levels during samples fabrication [23,24].

EDS analysis (Figs. 3a and 3b) revealed that the samples sintered at 1550 °C for 2 h in an air atmosphere obtained by both methods possess chemical composition similar to the nominal one [26]. EDS analysis results of the compositions are shown in Table 3. Eventually, the obtained results indicated that the sintered samples based on CeO_2 remained structurally and chemically stable keeping composition almost identical to nominal, regardless of applying a high temperature of over 1500 °C during the sintering process [26]. Most importantly, the confirmed high thermal stability of investigated ceramics makes them promising candidates for application as solid electrolytes in IT-SOFCs.

Table 3. Ion fractions in the ceramic samples CNSGDY sintered for 2 h at 1550 °C in an air atmosphere obtained by MGNP and SPRT methods

Composition	Ion fractions [%]					
	Ce	Nd	Sm	Gd	Dy	Y
CNSGDY (MGNP method)	78.71	0.33	0.30	4.79	6.25	9.62
CNSGDY (SPRT method)	78.82	0.32	0.35	5.36	6.67	8.50

3.3. Electrical conductivity

As commonly known, the application complex electrochemical impedance spectroscopy (EIS) is well developed technique for characterization of the electrical properties of solid electrolytes based on the interfacial reaction at the electrode surface [19,21,23–25,30–35]. Besides the total conductivity values, it provides useful information related to the contribution of grains' interior, grain boundaries, and electrode-electrolyte interface to the overall ionic conductivity [23–25].

Nyquist plots of the sintered CNSGDY samples obtained by MGNP and SPRT methods, recorded within the temperature range of 500–700 °C with the increments of 50 °C, are presented in Fig. 4. In comparison to previously reported results [23–25,35], on average, our samples showed the highest conductivity. Their

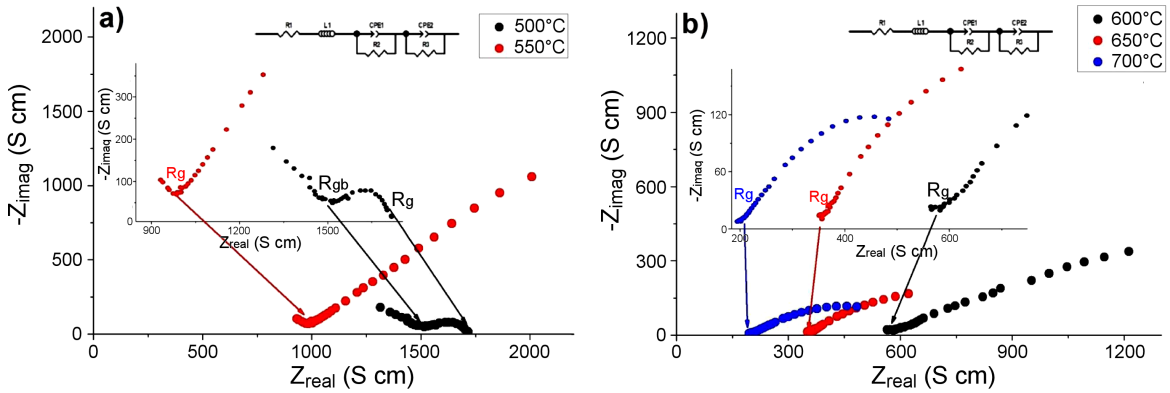

Figure 4. Complex impedance plots of the sintered CNSGDY samples obtained by MGNP method measured in the temperature range from 500–700 °C in an air atmosphere (temperatures are indicated at each diagram and arrows indicate the points on the real axis corresponding to the readings of R_g, R_{gb} and $R_g + R_{gb}$)

original Nyquist plots for various temperatures were selected to illustrate the impedance behaviour of the investigated group of doped ceria samples as a whole [23–25,35]. In this case, Nyquist plots were fitted with the equivalent circuit consisting of two serially connected parallel circuits which both contained one resistive and one distributed (frequency dependent) capacitive elements. Such equivalent circuit with both constant and distributed capacitive elements was applied in plenty of scientific papers concerning sintered ceramics [23–25,35]. The high-frequency semicircle may be attributed to a parallel connection of the bulk resistance (R_g) of crystalline grains and the geometric capacitance (C_g) of the sample. If the impedance semicircles are clearly separated, i.e. $R_gC_g \ll R_{gb}C_{gb}$, the values of R_g and R_{gb} may be read separately as a low-frequency intercepts of the semicircles with the real axis. By defining frequency corresponding to the high-frequency semicircle maximum, $\omega_{max,g}$, geometric capacitance can be calculated according to the equation:

$$\omega_{max,g} = \frac{1}{R_gC_g} \tag{5}$$

where $\omega_{max,g}$ is frequency corresponding to the high-frequency semicircle maximum.

The low-frequency semicircle may be attributed to the grain boundary resistance (R_{gb}) in parallel connection with the intergranular capacitance (C_{gb}) [23–25]. In this case, based on frequency referring to the semicircle maximum ($\omega_{max,gb}$), intergranular capacitance can be calculated with the following equation:

$$\omega_{max,gb} = \frac{1}{R_{gb}C_{gb}} \tag{6}$$

As indicated, the spectrum presented in Fig. 4a at 500 °C is composed of two semicircles which could be confidently attributed to bulk and grain boundary responses. The values R_g and R_{gb} were estimated in the available frequency range from the experimental cross section of obtained semicircles with the Z_{real} (a real component of impedance), where both intersection points were marked with black arrows [23–25,35]. The exact semicircles corresponding to either grain or grain boundaries appeared only when the grains are distributed uniformly [35]. The bulk semicircle occurred in the higher frequency region, and the grain boundary semicircle may be found in the intermediate frequency region [35]. However, with the temperature increase, as indicated in Fig. 4a at 550 °C, both resistance elements (R_g and R_{gb}) obviously decrease, which causes an increase in ω_{max}. Consequently, the whole region of the impedance points shifts towards the low-frequency semicircle. We noticed a similar thing in Fig. 4b in the temperature range of 600–700 °C. Namely, at higher temperatures, the time constants associated with the bulk and grain boundary impedances are much lower than those associated with the electrode interface [23–25,35]. As a result, the semicircles due to bulk and grain boundary gradually disappear and only a single semicircle can be observed (Fig. 4a at 550 °C and Fig. 4b). Thus, instead of R_g and R_{gb} separately, only the whole sum $R_g + R_{gb}$ became readable from the experimental cross section of obtained semicircles with the real component of impedance (Z_{real}) [22–24], in the available frequency range. These results indicate that the dopant concentration and temperatures have a great influence on the bulk and grain boundary semicircles causing the decrease in bulk and grain boundary resistances. This was expected since the grain boundary semicircle is dependent on the microstructure of the pellet, particularly on the grain size. In addition, it has already been shown that the grain size and grain size distribution were changed with the increase in dopant concentration [23–25,35].

The electrode/electrolyte contribution to the overall electrolyte resistance has not been considered in this work because the total resistance of electrolyte is given by the sum of grain (R_g) and grain boundary resistance (R_{gb}) [23–25]. A new semicircle that is highly visible in a low-frequency region in the temperature range 600–700 °C (Fig. 4b) originates from the oxygen electrode reactions, O_2/O^{2-} [23, 24], which does not belong to the scope of this study.

Table 4. Grain (σ_g) and grain boundary (σ_{gb}) conductivities at 500 °C, and total conductivity measured in the temperature range 550–700 °C of the sintered ceramic samples CNSGDY obtained by the MGNP and SPRT methods

Temperature [°C]	Composition			
	CNSGDY (MGNP method)		CNSGDY (SPRT method)	
	σ_g [S cm^{-1}]	σ_{gb} [S cm^{-1}]	σ_g [S cm^{-1}]	σ_{gb} [S cm^{-1}]
500	0.99×10^{-3}	0.63×10^{-3}	0.87×10^{-3}	0.69×10^{-3}
	σ_{total} [S cm^{-1}]		σ_{total} [S cm^{-1}]	
550	0.88×10^{-3}		0.72×10^{-3}	
600	1.02×10^{-2}		0.87×10^{-3}	
650	1.36×10^{-2}		0.96×10^{-3}	
700	4.22×10^{-2}		1.31×10^{-2}	

The total conductivities of both sintered samples obtained by MGNP and SPRT methods, measured in the temperature range of 500–700 °C are presented in Table 4. It is interesting that the actual values of the conductivity of grain (σ_g) and grain boundary (σ_{gb}) of the above mentioned samples can be read only at 500 °C (Table 4; grain (σ_g): 0.99×10^{-3} S cm^{-1} and 0.87×10^{-3} S cm^{-1}, grain boundary (σ_{gb}): 0.63×10^{-3} S cm^{-1} and 0.69×10^{-3} S cm^{-1}, for MGNP and SPRT, respectively). However, with the temperature increase, it was possible to determine only the values of total conductivity of both sintered ceramic CNSGDY samples (Table 4). The reason for this may be in non-uniformly distributed grain and grain boundaries [36], which can be clearly seen in Figs. 2a,b. The highest values of the total conductivity of the samples were reached at 700 °C, amounting to 4.22×10^{-2} S cm^{-1} and 1.31×10^{-2} S cm^{-1}, for MGNP and SPRT, respectively.

Further, comparing the obtained results of total conductivity at 700 °C for both sintered ceramic CNSGDY samples with results found in our previous paper [24], it can be noted that these values are almost two times higher. Moreover, the values of total conductivity that have been achieved in the present work at 700 °C are similar to the results by other authors [25,36] obtained at higher temperature (800 °C). Even values of con-

Table 5. Comparison of total conductivity (σ) and activation energy (E_a) values at 600 and 700 °C for different electrolyte materials with dopants concentration of 20%, at different sintering conditions

Electrolyte material – synthesis method (sintering conditions)	σ at 600 °C [S cm^{-1}]	E_a at 600 °C [eV]	σ at 700 °C [S cm^{-1}]	E_a at 700 °C [eV]	Reference
CNSGDY – MGNP (1550 °C for 2 h)	$1.02 \cdot 10^{-3}$	0.26	$4.22 \cdot 10^{-2}$	0.26	this work
CNSGDY – SPRT (1550 °C for 2 h)	$0.87 \cdot 10^{-3}$	0.28	$1.31 \cdot 10^{-2}$	0.28	this work
$Ce_{0.8}Ga_{0.05}Cu_{0.15}O_{1.825}$ – auto combustion (1300 °C for 4 h)	$8.10 \cdot 10^{-3}$	0.62	$2.03 \cdot 10^{-2}$	0.62	[12]
$Ce_{0.85}Er_{0.15}O_{2-\delta}$ – SPRT (1550 °C for 2 h)	$4.46 \cdot 10^{-3}$	0.28	$1.10 \cdot 10^{-2}$	0.28	[23]
$Ce_{0.8}Sm_{0.08}Gc_{0.12}O_{2-\delta}$ – SPRT (1550 °C for 2 h)	$1.03 \cdot 10^{-2}$	0.23	$1.92 \cdot 10^{-2}$	0.23	[24]
$Ce_{0.8}Sm_{0.08}Gc_{0.12}O_{2-\delta}$ – MGNP (1550 °C for 2 h)	$1.07 \cdot 10^{-2}$	0.24	$2.14 \cdot 10^{-2}$	0.24	[24]
$Ce_{0.8}Gd_{0.14}Mg_{0.06}O_{1.9-\delta}$ – sol-gel (1300 °Cfor 4 h)	$3.4 \cdot 10^{-3}$	0.85	$1.58 \cdot 10^{-2}$	0.85	[25]
$Ce_{0.8}Nd_{0.01}Sm_{0.04}Gd_{0.04}Dy_{0.04}Y_{0.07}O_{2-\delta}$ – MGNP (1500 °C for 1 h)	$6.44 \cdot 10^{-2}$	0.72	$1.40 \cdot 10^{-2}$	0.72	[30]
$Ce_{0.8}Nd_{0.01}Sm_{0.04}Gd_{0.04}Dy_{0.04}Y_{0.07}O_{2-\delta}$ – SPRT (1500 °C for 1 h)	$1.18 \cdot 10^{-3}$	0.59	$2.19 \cdot 10^{-2}$	0.59	[30]
$Ce_{0.8}Sm_{0.1}Er_{0.1}O_{2-\delta}$ – sol-gel-assisted citric acid-nitrate combustion (1400 °C for 5 h)	$1.12 \cdot 10^{-2}$	0.66	$2.251 \cdot 10^{-2}$	0.47	[31]
$Ce_{0.8}Sm_{0.05}B_{0.15}O_2$ – solid state reaction (800 °C for 10 h)	/	/	$7.46 \cdot 10^{-4}$	0.5447	[32]
$Cu_{0.08}Mn_{0.02}Zr_{0.1}Ce_{0.8}O_2$ – co-precipitation (1150 °Cfor 4 h)	$8 \cdot 10^{-2}$	0.37	/	0.37	[33]
$Ce_{0.8}Er_{0.2}O_{2-\delta}$ – sol-gel-assisted citric acid-nitrate combustion (1500 °C for 6 h)	$8.23 \cdot 10^{-3}$	0.55	$1.822 \cdot 10^{-2}$	0.55	[34]
$Ce_{0.8}Sm_{0.2}Li_{0.05}O_{1.825}$ – citrate-nitrate combustion (900 °C for 5 h)	/	/	$1.81 \cdot 10^{-3}$	0.80	[37]

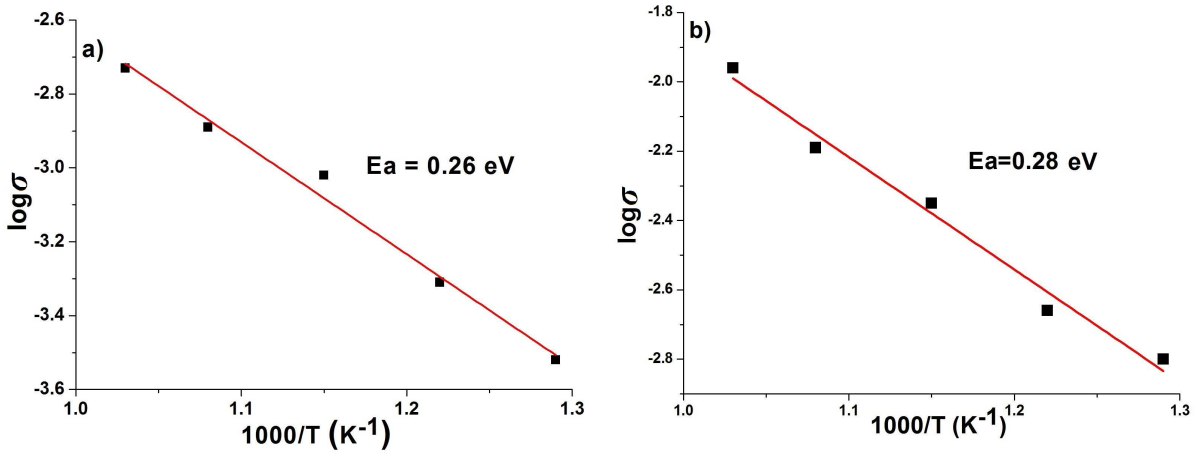

Figure 5. The dependence of the $\log \sigma = f(1/T)$ for the CNSGDY sintered samples obtained by MGNP and SPRT methods

ductivity obtained and presented in literature at 700 °C [35,37] are lower compared to the results in this investigation at temperatures of 500 and 600 °C. In order to compare, Table 5 presents the values of conductivity at 600 °C with the corresponding activation energy. It can be clearly concluded that the obtained results for the SPRT samples are in the similar range as literature data, while for the MGNP samples they are noticeably higher. With the further comparison of the values for conductivity obtained for similar materials based on oxygen ion conductors (multi-doped ceria materials) investigated in previous literature reports [12,19,20,24,25,30–34,37], it may be observed that present results for the SPRT samples are in the similar range while for the MGNP samples are noticeably higher. What is more, referring to some existing studies [32,38], the present results are higher for a whole order of magnitude even for the SPRT samples.

Finally, the advantages of MGNP and SPRT methods, such as better control of the chemical reaction and more precise stoichiometry of the final product in comparison to a tailored composition, should be emphasized. Furthermore, these methods stand for very fast and reliable ones, whereas extremely simple and low-cost equipment required makes them even more convenient and cost-effective. Also, it is important to note that in addition to various dopant concentrations, the ceramic samples studied in our work displayed the difference in density, grain size and porosity, which also may influence the ionic conductivity.

According to the results listed in Table 4, the dependence $\log \sigma = f(1/T)$ for the MGNP and SPRT sintered CNSGDY samples are presented in Fig. 5. Activation energies (E_a) were calculated from the slopes of the Arrhenius plots according to the derived equation:

$$\ln(\sigma \cdot T) = \ln A - \frac{E_a}{k} \cdot \frac{1}{T} \tag{7}$$

where σ is the conductivity, T is the absolute temperature, A is the pre-exponential factor and k is the Boltzmann constant. Ionic conduction is a thermally activated process which is the reason why it is affected by temperature [30]. Activation energies of total conduction for the sintered MGNP and SPRT samples with CNSGDY composition were determined to be 0.26 and 0.28 eV, respectively.

In comparison with activation energies of similar materials from the published studies of different authors on oxygen ion conductors based on either single-, co- and multi-doped CeO_2 containing dopant concentration in the range of 15–20 mol% [12,25,30–34,37], E_a values obtained in this work were significantly lower. However, it could be noted that results for activation energy in the present study were similar to the values obtained in our previous studies [23,24] where nanosized samples of composition $Ce_{0.8}Sm_{0.08}Gd_{0.12}O_{2-\delta}$ were obtained by following the same procedures (SPRT and MGNP methods) which indicated the benefits of their application for electrolytes production. As a matter of fact, it may be assumed this is a consequence of well-ordered structure and better processability of the nanopowders obtained by MGNP and SPRT methods during the sintering process, which allows easier activation of conductivity carriers [23,24,30]. Nonetheless, the activation energy of the MGNP sample compared to the one of the SPRT sample is found to be slightly lower at all temperatures which may be explained by the higher grains surface area of MGNP samples [30]. A detailed literature review containing results of total conductivity and corresponding activation energy values for different electrolyte materials based on co- and multi-doped ceria at 700 °C with dopant concentration in the range of 15–20 mol% is presented in Table 5. Considering rather high sintering temperature, it can be assumed that obtained ceria ceramics exhibit high thermal stability, which is favourable considering their potential use as perspective solid ionic conductors operating at intermediate and high temperatures of SOFC.

IV. Conclusions

The multi-doped ceria with CNSGDY composition has been synthesized by modified glycine-nitrate pro-

cedure (MGNP) and self-propagating room temperature method (SPRT) and subjected to sintering process at 1550 °C for 2 h in air atmosphere. From results obtained by XRPD analysis, it may be concluded that all sintered samples have cubic fluorite structure with the space group Fm3m, similar to pure CeO_2, while no secondary phases besides the ceria phase were formed after sintering. Additionally, XRPD confirmed that the particle size of samples lays in the nanometric range. FE-SEM analysis revealed that the sintered samples possessed a bimodal size distribution with grain size in the range of 1–4 μm. In the compositions of the fine oxide, CNSGDY samples achieved relative densities of 96 %TD (MGNP) and 89 %TD (SPRT) after sintering at 1550 °C. The maximal total conductivity values measured by the complex impedance method using electrochemical impedance spectroscopy were 4.22×10^{-2} and 1.31×10^{-2} S cm^{-1} at 700 °C, obtained for the MGNP and SPRT samples, respectively. Bearing in mind that straightforward and low-cost procedures were followed for powders fabrication, the present study brought to the conclusion that examined materials could have great application potential in IT-SOFC technology as solid electrolytes. However, additional investigations primarily aimed at the improvement of certain properties of such materials in terms of the increase of density and ionic conductivity, are needed to be the focus of future research.

Acknowledgements: These investigations were supported by the Ministry of Education, Science and Technological Development of the Republic of Serbia (Contract numbers 451-03-495 68/2022-14/200017) through the realization of research themes 1702203 and 1702205.

References

1. R.O. Da Fonseca, R.C. Rabelo-Neto, R.C.C. Simões, L.V. Mattos, F.B. Noronha, "Pt supported on doped CeO_2/Al_2O_3 as catalyst for dry reforming of methane", *Int. J. Hydrog. Energy*, **45** [8] (2020) 5182–5191.
2. Y. Liang, X. Ding, J. Wang, M. Zhao, Y. Dan, L. Jiang, Y. Chen, "Comparative activity and hydrothermal stability of FeO_x- and CeO_2-doped Pt-based catalysts for eliminating diesel emissions", *J. Environ. Chem. Eng*., **8** [5] (2020) 104361.
3. J. Zhang, L. Wang, X. Hu, Q. Shao, X. Xu, C. Long, "Balancing surface acidity, oxygen vacancies and Cu^+ of CuO_x/CeO_2 catalysts by Nb doping for enhancing CO oxidation and moisture resistance and lowering byproducts in plasma catalysis", *J. Clean. Prod.,* **318** (2021) 128564.
4. H.M. Albert, T. Lohitha, K. Alagarsamy, C.A. Gonsago, V. Vishwakarma, "Performance of $ZnSO_4$ doped CeO_2 nanoparticles and their antibacterial mechanism", *Mater. Today Proc*., **47** (2021) 1030–1034.
5. H. Yang, B. Xu, Q. Zhang, S. Yuan, Z. Zhang, Y. Liu, T. Ohno, "Boosting visible-light-driven photocatalytic performance of waxberry-like CeO_2 by samarium doping and silver QDs anchoring", *Appl. Catal. B Environ*., **286** (2021) 119845.
6. L. Song, T. Xu, D. Gao, X. Hu, C. Li, S. Li, G. Chen, "Metal-organic framework (MOF) derived carbon mediated interfacial reaction for the synthesis of CeO_2-MnO_2", *Catalysts. Chem. Eur. J*., **25** (2019) 6621–6627.
7. P. Patil, U.T. Nakate, K. Harish, S.P. Pavan, N.P. Rakesh, D. Selvakumar, N.S. Kumar, "Au sensitized La-CeO_2 catalyst coated ceramics monoliths for toluene catalysis application", *Mater. Chem. Phys.,* **240** (2020) 122269.
8. D.H. Leea, K.S. Chaa, Y.S. Leea, K.S. Kangb, C.S. Parkb, Y.H. Kima, "Effects of CeO_2 additive on redox characteristics of Fe–based mixed oxide mediums for storage and production of hydrogen", *Int. J Hydrogen Energy*, **34** [3] (2019) 1417–1422.
9. G. Zhang, X.U. Jianyi, H.O. Zhonghui, W.A. Qingchun, "Research on micro–structure and catalysis properties of nanosized Ce_{1-x} $(Fe_{0.5}Eu_{0.5})_xO_{2-\delta}$ solid solutions", *J. Rare Earths*, **35** [1] (2017) 63–70.
10. L. Fan, J. Zhang, K. Ma, Y. Zhang, Y.M. Hu, L. Kong, J.Q. Lu, "Ceria morphology-dependent Pd-CeO_2 interaction and catalysis in CO_2 hydrogenation into formate", *J. Catalysis*, **397** (2021) 116–127.
11. H. Shi, C. Su, R. Ran, J. Cao, Z. Shao, "Electrolyte materials for intermediate-temperature solid oxide fuel cells", *Prog. Nat. Sci. Mater. Int*., **30** [6] (2020) 764–774.
12. M. Singh, A.K. Singh, "Studies on structural, morphological, and electrical properties of Ga^{3+} and Cu^{2+} co-doped ceria ceramics as solid electrolyte for IT-SOFCs", *Int. J. Hydrog. Energy*, **45** [44] (2019) 24014–24025.
13. S. Hussain, Y. Li, A. Mustehsin, A. Ali, K.H. Thebo, Z. Ali, S. Hussain, "Synthesis and characterization of ZnO/samarium-doped ceria nanocomposites for solid oxide fuel cell applications", *Ionics*, **27** (2021) 4849–4857.
14. S. Hussain, Y. Li, F.H. Memon, S. Hussain, L. Li, K.H. Thebo, "Studies on he effects of pre-firing and sintering temperature on NSDC nanocomposite electrolytes", *Prog. Nat. Sci. Mater. Int*., **32** [1] (2022) 128–134.
15. J. Park, H. Lee, Y. Lim, S.W. Kong, P.C. Su, Y.B. Kim, "Sub-second sintering process for $La_6Sr_4Co_2Fe_8O_{3-\delta}$-gadolinium doped ceria composite cathode via a flash light irradiation method for intermediate temperature-solid oxide fuel cells", *J. Alloys Compd*., **895** (2022) 162683.
16. K. Venkataramana, C. Madhuri, C.V. Reddy, "Triple-doped ceria-carbonate ($Ce_{0.82}La_{0.06}Sm_{0.06}Gd_{0.06}O_{2-\delta}$–$(Li–Na)_2CO_3$) nanocomposite solid electrolyte materials for LT-SOFC applications", *Ceram. Int*., **46** [17] (2020) 27584–27594.
17. S. Dwivedi, "Solid oxide fuel cell: Materials for anode, cathode and electrolyte", *Int. J. Hydrog. Energy*, **45** [44] (2020) 23988–24013.
18. H.Y. Lai, Y.H. Chan, "Enhancement of ion conductivity for doped electrolytes in SOFC by MD modeling", *Comput. Mater. Sci.*, **144** (2018) 265–272.
19. C. Madhuri , K. Venkataramana, J. Shanker, C.V. Reddy, "Effect of La^{3+},Pr^{3+}, and Sm^{3+} triple-doping on structural, electrical, and thermal properties of ceria solid electrolytes for intermediate temperature solid oxide fuel cells", *J. Alloys Compd*., **849** (2020) 15663.
20. S.Y. Toor, E. Croiset, "Reducing sintering temperature while maintaining high conductivity for SOFC electrolyte: copper as sintering aid for samarium doped ceria", *Ceram. Int*., **46** [1] (2020) 1148–1157.
21. M. Stojmenović, S. Bošković, S. Zec, B. Babić, B. Matović, D. Bučevac, Z. Dohčević–Mitrović, F. Aldinger,

"Characterization of nanometric multidoped ceria powders", *J Alloys Compd.*, **507** [1] (2010) 279–285.
22. M. Stojmenović, M.C. Milenković, P.T. Banković, M Žunić, J.J. Gulicovski, J.R. Pantić, S.B. Bošković, "Influence of temperature and dopant concentration on structural, morphological and optical properties of nanometric $Ce_{1-x}Er_xO_{2-\delta}$ (x = 0.05–0.20) as a pigment", *Dyes Pigments*, **123** (2015) 116–124.
23. M. Stojmenović, S. Bošković, M. Žunić, B. Babić, B. Matović, D. Bajuk-Bogdanović, S. Menus, "Studies on structural, morphological and electrical properties of $Ce_{1-x}Er_xO_{2-\delta}$ (x = 0.05–0.20) as solid electrolyte for IT-SOFC", *Mater. Chem. Phys.*, **153** (2015) 422–431.
24. M. Stojmenović, M. Žunić, J. Gulicovski, D. Bajuk-Bogdanović, I. Holclajtner-Antunović, V. Dodevski, S. Menus, "Structural, morphological, and electrical properties of doped ceria as a solid electrolyte for intermediate–temperature solid oxide fuel cells", *J. Mater. Sci.*, **50** [10] (2015) 3781–3794.
25. J. Cheng, C. Tian, J. Yang, "Effects of Mg^{2+} addition on structure and electrical properties of gadolinium doped ceria electrolyte ceramics", *Process. Appl. Ceram.*, **13** [2] (2019) 182–188.
26. M. Stojmenović, M.C. Pagnacco, V. Dodevski, J. Gulicovski, M. Žunić, S. Bošković, "Studies on structural and morphological properties of multidoped ceria $Ce_{0.8}Nd_{0.0025}Sm_{0.0025}Gd_{0.005}Dy_{0.095}Y_{0.095}O_{2-\delta}$ ($x = 0.2$) as solid solutions", *J. Spectroscopy*, **2016** (2016) 5184542.
27. D. Mićović, M.C. Pagnacco, P. Banković, J. Maletaškić, B. Matović, V. Đokić, M. Stojmenović, "The influence of short thermal treatment on structure, morphology and optical properties of Er and Pr doped ceria pigments: Comparative study", *Process. Appl. Ceram.*, **13** [3] (2019) 310–321.
28. C. Solís, M. Balaguer, J.M. Serra, "In situ Raman characterization of SOFC materials in operational conditions: A doped ceria study", *Membranes*, **10** [7] (2020) 148.
29. P.P. Ortega, B. Hangai, H. Moreno, L.S. Rocha, M.A. Ramírez, M.A. Ponce, E. Longo, A.Z. Simões, "Tuning structural, optical, and gas sensing properties of ceria-based materials by rare-earth doping", *J. Alloys Compd.*, **888** (2021) 161517.
30. M. Stojmenović, S. Bošković, M. Žunić, J.A. Varela, M. Prekajski, B. Matović, S. Mentus, "Electrical properties of multidoped ceria", *Ceram. Int.*, **40** [7] (2014) 9285–9292.
31. M. Anwar, Muhammed Ali S.A., N.A. Baharuddin, N.F. Raduwan, A. Muchtar, M.R. Somalu, "Structural, optical and electrical properties of $Ce_{0.8}Sm_{0.2-x}Er_xO_{2-\delta}$ (x = 0–0.2) co-doped ceria electrolytes", *Ceram. Int.*, **44** [12] (2018) 13639–13648.
32. K. Sandhya, N.S. ChitraPriya, P.K. Aswathy, D.N. Rajendran, "Electrical properties of rare earth doped ceria electrolyte for solid oxide fuel cell applications", *Mater. Today Proc.*, **10** (2019) 112–120.
33. I.V. Zagaynov, S.V. Fedorov, M.A. Goldberg, "Electrical properties of Cu-Mn-Zr co-doped ceria electrolytes for intermediate temperature solid oxide fuel cell application", *Process. Appl. Ceram.*, **13** [3] (2019) 244–249.
34. M. Anwar, Muhammed Ali S.A., A. Muchtar, M.R. Somalu, "Influence of strontium co-doping on the structural, optical, and electrical properties of erbium-doped ceria electrolyte for intermediate temperature solid oxide fuel cells", *Ceram. Int.*, **45** [5] (2019) 5627–5636.
35. M. Stojmenović, M. Žunić, J. Gulicovski, V. Dodevski, M. Prekajski, A. Radulović, S. Mentus, "Structural, morphological and electrical properties of $Ce_{1-x}Ru_xO_{2-\delta}$ (x = 0.005–0.02) solid solutions", *Ceram. Int.*, **42** [12] (2016) 14011–14020.
36. J. Wright, A.V. Virkar, "Conductivity of porous Sm_2O_3–doped CeO_2 as a function of temperature and oxygen partial pressure", *J. Power Sources*, **196** [15] (2011) 6118–6124.
37. S. Preethi, M. Abhiroop, K.S. Babu, "Low temperature densification by lithium co-doping and its effect on ionic conductivity of samarium doped ceria electrolyte", *Ceram. Int.*, **45** [5] (2019) 5819–5828.
38. R. Kirkgeçit, H.Ö. Torun, "Synthesis and characterization of $CeLaMO_2$ (M: Sm, Gd, Dy) compounds for solid ceramic electrolytes", *Process. Appl. Ceram.*, **14** [4] (2020) 314–320.